Diagn Interv Radiol 2015; 21: 293–306

CHEST IMAGING

REVIEW

Imaging the posterior mediastinum: a multimodality approach

Mariaelena Occhipinti
Benedikt H. Heidinger
Elisa Franquet
Ronald L. Eisenberg
Alexander A. Bankier

ABSTRACT
The posterior mediastinum contains several structures that can produce a wide variety of pathologic conditions. Descending thoracic aorta, esophagus, azygos and hemiazygos veins, thoracic duct, lymph nodes, adipose tissue, and nerves are all located in this anatomical region and can produce diverse abnormalities. Although chest radiography may detect many of these pathologic conditions, computed tomography and magnetic resonance are the imaging modalities of choice for further defining the relationship of posterior mediastinal lesions to neighboring structures and showing specific imaging features that narrow the differential diagnosis. This review emphasizes modality-related answers to morphologic questions, which provide precise diagnostic information.

The posterior mediastinum is the anatomical region bordered superiorly by the thoracic inlet, inferiorly by the diaphragm, anteriorly by the pericardium and the great mediastinal vessels, posteriorly by the anterior longitudinal ligament, and laterally by the right and left parietal pleura folds (1). It contains the descending thoracic aorta, esophagus, azygos and hemiazygos veins, thoracic duct, lymph nodes, adipose tissue, vagus and splanchnic nerves, and autonomic ganglia. Based on these various anatomical structures, a wide variety of pathologic conditions can be located in the posterior mediastinum (Table 1). Many of these conditions can be detected by chest radiography (CXR). However, computed tomography (CT) and magnetic resonance imaging (MRI) are the imaging modalities of choice for further defining their relationship with neighboring structures, as well as for revealing specific imaging features that might narrow the differential diagnosis.

This article presents specific imaging features of individual disorders of the posterior mediastinum. To streamline the imaging algorithms for these conditions the article emphasizes modality-related answers to morphologic questions that can provide more precise diagnostic information.

Spine and nervous system

Neurogenic tumors

Up to 95% of neurogenic tumors occur in the posterior mediastinum, and they are the most common posterior mediastinal masses (2, 3). According to the cell of origin, neurogenic tumors are divided into three groups: nerve sheath tumors, sympathetic ganglion cell tumors, and paraganglionic cell tumors.

Nerve sheath tumors are the most common type of neurogenic tumors in adults (3, 4). They include benign schwannomas and neurofibromas, as well as malignant peripheral nerve sheath tumors. Sympathetic ganglion tumors, the most common type in children (3, 4), have various histologic grades of aggressiveness. Ganglioneuroma is considered as benign, despite its potential to metastasize. Ganglioneuroblastoma has intermediate aggressiveness, and neuroblastoma is the most aggressive form. Paraganglionic cell tumors in the posterior mediastinum are rare and arise along the sympathetic chain, in the so-called aortosympathetic paraganglia (5).

On CXR, the smoothly rounded or oval opacities caused by neurogenic tumors obliterate the paraspinal lines and can be associated with scalloping of the adjacent bones (5). On CT, the sharply defined soft-tissue masses in the paravertebral area have variable appearance, ranging from an iso- or hypoattenuating mass (Fig. 1) to heterogeneous lesions containing

From the Department of Radiology (A.A.B ✉ *abankier@bidmc.harvard.edu*), Harvard Medical School, Beth Israel Deaconess Medical Center, Boston, Massachusetts, USA.

Received 11 November 2014; revision requested 7 December 2014; revision received 24 December 2014; accepted 29 December 2014.

Published online 15 May 2015.
DOI 10.5152/dir.2014.14467

hemorrhage, necrosis, cystic degeneration, calcifications, and patchy fat areas (Fig. 2) (6, 7). CT is superior to CXR in demonstrating erosion or scalloping of adjacent ribs and vertebral bodies. In tumors extending through the intervertebral foramina, CT also shows the typical "dumbbell" appearance (3). After contrast injection, small paragangliomas show avid and homogeneous enhancement, whereas ganglioneuromas show subtle enhancement in the arterial phase and mild enhancement in the delayed phase (5, 6). No typical enhancement characteristics have been reported for other types of neurogenic tumors. Rapid growth, necrosis, and hemorrhage are CT findings suggestive of malignancy. Finally, CT is the imaging modality used for assessing distant metastases to bone, lung, and liver, as commonly seen in neuroblastomas (3, 4, 8).

MRI helps to differentiate between individual neurogenic tumors. Paragangliomas show a characteristic "salt-and-pepper" appearance on T1-weighted images, due to the presence of multiple curvilinear and punctate signal voids that correspond to high-velocity flow in intratumoral vessels (9). Conversely, on T2-weighted images, ganglioneuromas may present a "whorled" appearance (Fig. 2) (6, 10) and neurofibromas may show a "target" pattern, defined as a central portion with lower signal intensity than the peripheral zone (5, 11). MRI accurately demonstrates the presence and extent of intraspinal tumor, invasion of adjacent neural structures, and encasement of vessels, which influence surgical treatment and management (3).

Metaiodobenzylguanidine scintigraphy is highly sensitive for determining the extent of disease in catecholamine-producing neuroblastomas and paragangliomas. ^{18}F-fluorodeoxyglucose positron emission tomography (^{18}F-FDG-PET) scanning has reasonable accuracy (82%) in distinguishing malignant forms from benign forms.

Main points

- Posterior mediastinal lesions can be classified according to their anatomic origin.
- CT and MRI are the imaging modalities of choice for revealing specific imaging features as well as defining the relationship with neighboring structures and any spread of neoplastic disease.
- We created modality-related answers to morphologic questions that can provide definite diagnostic information and help in daily clinical practice.

Infectious spondylitis

Infectious spondylitis is usually caused by pyogenic or tuberculous infection, the latter known as Pott's disease (4). Hematogenous spread is the most common pathway of infectious spondylitis, though direct inoculation, contiguous extension, or lymphatic drainage from adjacent affected areas may also occur. Infection of a vertebral body may extend into the pre- and paravertebral soft tissues, spreading via the anterior or posterior longitudinal ligaments (Fig. 3) (12, 13).

Early stages of paravertebral abscesses and bone destruction may be difficult to detect on CXR. Conversely, CT and MRI have a high sensitivity for detecting early osteolytic destruction of the vertebrae, accompanying focal or diffuse paraspinal soft-tissue abscess, intervertebral disc involvement, and epidural granulation tissue (4, 12).

Osteolytic destruction of the vertebrae may cause collapse, more commonly in the anterior part (Fig. 3), leading to the characteristic gibbus deformity in Pott's disease. Paravertebral soft-tissue abscess typically appears as a "horseshoe" mass surrounding an affected vertebral body. It may extend over several vertebral segments above and below the site of bone destruction. On CT, the abscess has soft-tissue density. On MRI, it has decreased signal intensity on T1-weighted images and increased signal intensity on T2-weighted images (Fig. 3) (14). Contrast material improves the detection of the paraspinal abscess on both CT and MRI. A pyogenic abscess usually has a thick and irregular enhancing wall, unlike the thin and smooth enhancement of the wall of a tuberculous abscess. Other features helpful in the differential diagnosis between tuberculous and pyogenic abscesses include calcifications in tuberculous infection and hypodensities or complete destruction of the intervertebral disc in pyogenic infection, which are best visual-

Table 1. Classification of the posterior mediastinal lesions according to the anatomic origin

Anatomic origin	Posterior mediastinal lesions
Spine and nervous system	Neurogenic tumors
	• Nerve sheath tumors
	• Sympathetic ganglion tumors
	• Paraganglionic cell tumors
	Infectious spondylitis
	Extramedullary hematopoiesis
	Meningocele
	Neuroenteric cyst
Vessels	Thoracic aortic aneurysm
	Aortic dissection
	Esophageal varices
	Dilated azygos vein
Esophagus	Esophageal neoplasms
	Esophageal duplication cyst
Lymph nodes	Lymphoma
	Lymphadenopathy
Adipose tissue	Lipoma and liposarcoma
	Mediastinal lipomatosis
Diaphragm	Hiatal hernia
	Bochdalek hernia
Extrathoracic lesions extending into mediastinum	Intrathoracic goiter
	Pancreatic pseudocyst

ized on CT (13, 15). In addition, MRI allows assessment of epidural masses with nerve root or spinal cord compression (Fig. 3).

The most important differential diagnosis is neoplasm, such as metastases, lymphoma, and multiple myeloma. Other differential diagnoses include sarcoidosis, Langerhans cell histiocytosis, and such rare spinal infections as brucellosis, mycosis, and echinococcosis (14, 16). Neoplasms usually spare the intervertebral disc, whereas inflammatory processes do not.

Imaging modalities can narrow the differential diagnosis and guide drainage or biopsy. Prompt treatment is crucial to limit spinal deformity and permanent neurologic deficit. Medical therapy should be integrated with surgical or CT-guided percutaneous catheter drainage of any paraspinal abscess (17). Treatment response to antibiotics can be evaluated by either CT, MRI, or ^{18}F-FDG-PET/CT.

Extramedullary hematopoiesis

Long-standing anemia or extensive bone marrow replacement by myeloproliferative disorders elicit the expansion of hematopoietic tissue outside of the bone marrow and may lead to the development of mass-like lesions, most often in the paravertebral thoracic region (18).

More than 80% of patients with extramedullary hematopoiesis are asymptomatic, with the condition incidentally detected at imaging (19). Rarely, there may be pleural effusion, hemothorax, or respiratory failure. Cord compression can cause back pain, lower extremity weakness, numbness, and even paraplegia (20).

CXR shows smooth, well-delineated paraspinal masses (Fig. 4), which may be associated with trabeculated and widened ribs in patients with chronic anemia (19, 21). CT and MRI show well-defined, usually bilateral, paraspinal masses (Fig. 4), most commonly in the lower thoracic area (12). CT attenuation values and MRI signal intensity vary according to the grade of hematologic activity of the lesion. Active lesions usually have soft-tissue density on CT and intermediate signal intensity on both T1- and T2-weighted MRI. Inactive lesions have low or high attenuation values on CT, depending on the presence of fat or the iron content of the masses (Fig. 4). For the same reason, inactive lesions have high-signal intensity on both T1- and T2-weighted images if there is fatty replacement (Fig. 4), or low signal intensity with iron deposition (12, 21). Mild homogeneous enhancement on both CT and MRI is usually seen in active lesions, whereas a heterogeneous enhancing pattern is more common in inactive lesions because of iron deposition or fatty replacement (22). In rare cases of extension into the spinal canal, MRI is required for the evaluation of spinal cord compression, which may lead to irreversible neurologic damage if untreated (23).

Nuclear medicine imaging and CT-guided biopsy are reserved for atypical cases, such as in patients with a single lesion in the paravertebral area (18).

Therapy options, such as blood transfusion or hydroxyurea or radiation therapy, are influenced by the hematologic activity. Therefore, imaging modalities play an important role in therapeutic decision planning (21).

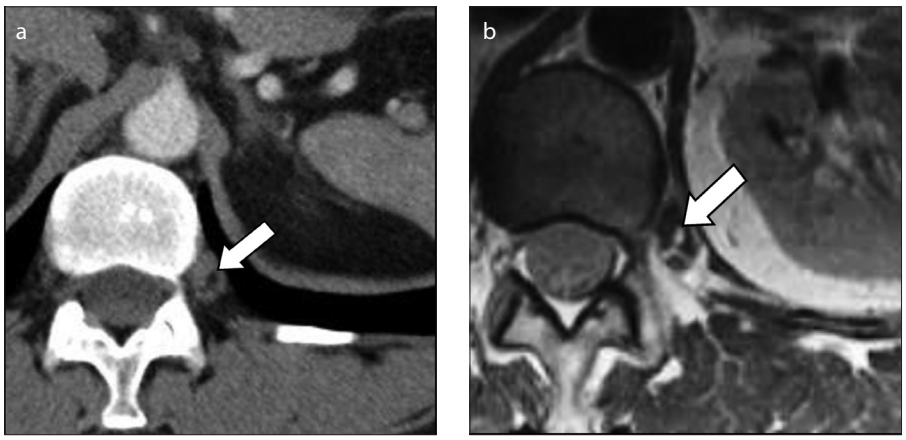

Figure 1. a, b. A 59-year-old male with multiple schwannomas. Axial CT scan **(a)** shows a paravertebral soft-tissue mass, with well-defined margins and low-attenuation central area *(arrow)* within the lesion. T2-weighted MRI **(b)** shows the mass with a central area of high signal intensity *(arrow)* surrounded by low-to-intermediate intensity signals.

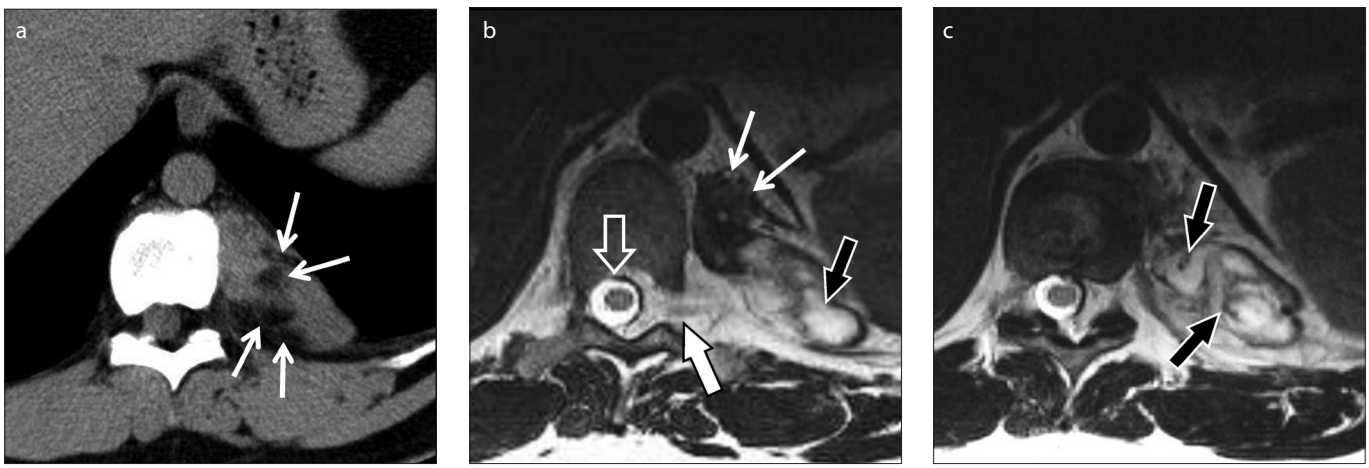

Figure 2. a–c. A 35-year-old male with ganglioneuroma. Axial unenhanced CT image **(a)** shows a paravertebral soft-tissue mass with patchy fat-attenuating areas *(arrows)*. Axial T2-weighted MRI **(b)** shows the mass with heterogeneous signal intensity, lower in the anterior portion *(thin white arrows)* and similar to cerebrospinal fluid in the most posterior part *(black arrow)*. Lesion widens towards adjacent intervertebral foramen *(thick white arrow)* and causes displacement of the thecal sac towards right *(open arrow)*. Axial T2-weighted MRI **(c)** shows curved hypointense signals *(arrows)* scattered among hyperintense signals, giving rise to a "whorled" appearance.

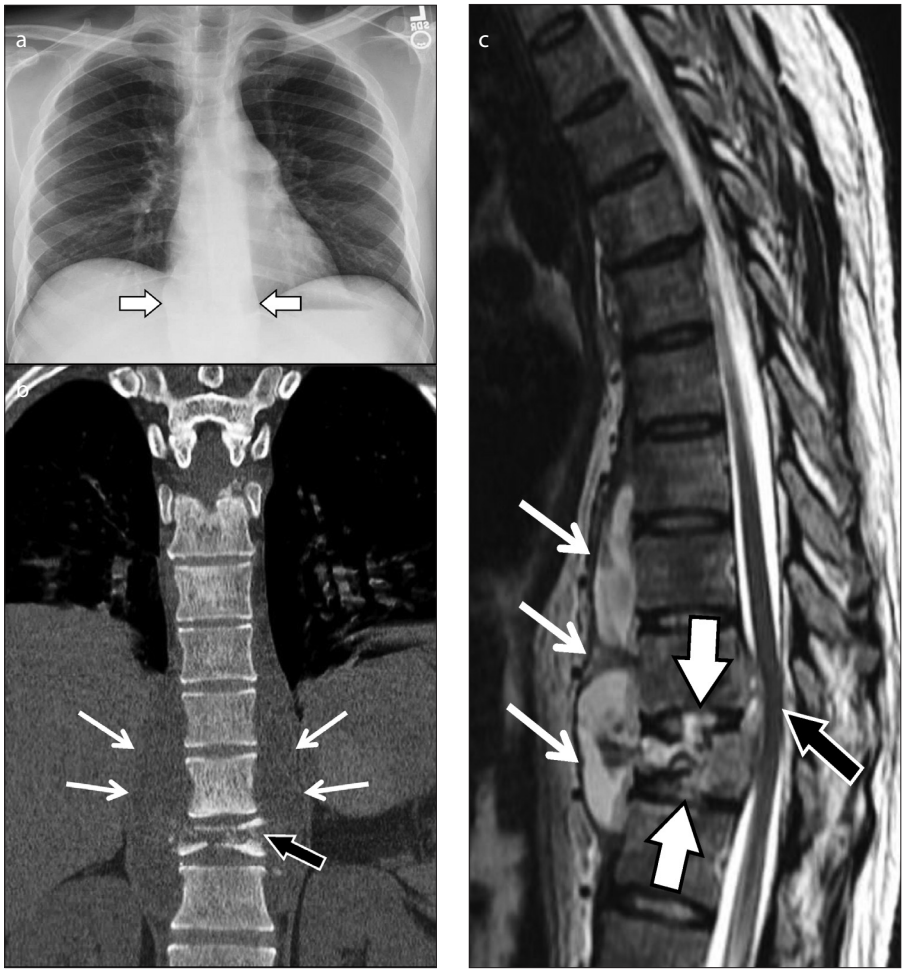

Figure 3. a–c. A 34-year-old male with Pott's disease. Posteroanterior chest radiography (CXR) **(a)** shows widening of both paraspinal lines *(arrows)* in lower third of the mediastinum. Coronal CT reformation **(b)** shows collapse of the vertebral body *(black arrow)* and craniocaudal extent of paravertebral abscess *(white arrows)*, which caused widening of paraspinal lines on CXR. Sagittal T2-weighted MRI **(c)** shows increased signal intensity within the affected vertebral body, adjacent intervertebral discs *(thick white arrows)*, and the paravertebral abscess *(thin white arrows)*. Abscess shows typical sub-ligamentous spread beneath anterior and posterior longitudinal ligaments, with posterior displacement and compression of the spinal cord *(black arrow)*. Sagittal image also reveals the gibbus deformity, caused by the collapse of the anterior part of the vertebral body.

Meningocele

Spinal meningocele is a saccular protrusion of the meninges through intervertebral foramina or bone defects in one or more vertebrae. Meningoceles contain cerebrospinal fluid and usually occur in the thoracic spine, especially between T3 and T7 (24). The protrusion can be anterior, lateral, anterolateral, or posterior to the vertebral body. Posterior meningoceles are the most common type, but they are not discussed in this review because they do not affect the posterior mediastinum.

Most meningoceles are associated with syndromes, such as neurofibromatosis type 1. Small meningoceles are asymptomatic and discovered incidentally on a routine CXR, whereas larger lesions may compress the spinal cord, spinal nerves, and adjacent mediastinal structures.

On CXR, meningoceles appear as paravertebral opacities with well-defined, smooth or lobulated borders. CT confirms a sharply defined, homogeneous, low-attenuation lesion up to 15 cm in diameter (25). The lesion protrudes from the spinal canal into the posterior mediastinum and has a right side predominance, possibly related to the aorta in the left side (24). CT also reveals abnormalities in adjacent vertebrae and enlargement of intervertebral foramina (25). On MRI, meningoceles are cystic masses with signal intensity of cerebrospinal fluid. This is the technique of choice for demonstrating connection of the lesion with the thecal sac, as well as for distinguishing a meningocele from a neurogenic tumor (26). Both CT and MRI are essential diagnostic tools to differentiate between coexisting lesions, such as neurinomas in patients with neurofibromatosis type 1.

Neuroenteric cyst

Foregut cysts include bronchogenic cysts, esophageal duplication cysts, and neuroenteric cysts (Table 2). Ninety percent of all neuroenteric cysts occur in the posterior mediastinum, more commonly above the level of the carina (3). Almost all neuroenteric cysts are diagnosed by one year of age, with infants usually presenting with such symptoms of tracheobronchial compression as dyspnea, stridor, and persistent cough (3). Occasionally, neuroenteric cysts are discovered in asymptomatic children (27). Surgery is the curative treatment reserved only for symptomatic neuroenteric cysts (27).

On CXR, neuroenteric cysts appear as solitary, rounded, well-defined mediastinal opacities. They can be associated with vertebral anomalies, which may be seen at a level different from that of the cyst (28).

On CT, neuroenteric cysts are homogeneous lesions of water attenuation with distinct borders. They can be connected to or extend into the spinal canal (3). CT allows better evaluation of vertebral anomalies, such as hemivertebrae, butterfly vertebrae, scoliosis, anterior spina bifida, and split notochord syndrome (27).

On MRI, neuroenteric cysts have high signal intensity on T2-weighted images and are usually of low signal intensity on T1-weighted sequences, because they contain cerebrospinal fluid (12). MRI is essential in the workup of a suspected neurogenic cyst because it can depict each anatomic relation to the spinal canal.

Vessels

Thoracic aortic aneurysm

An aortic aneurysm is defined as a permanent localized dilatation of the aorta, having at least a 50% increase in the expected normal diameter (29). The normal diameter of the mid-descending aorta in adults is 2.39–2.98 cm and 2.45–2.64 cm in males and females, respectively. The normal diameter of diaphragmatic aorta in adults is 2.43–2.69 cm and 2.40–2.44 cm in males and females, respectively (29). All these values increase with age. Aneurysms of the descending thoracic aorta represent 31%–37% of all aortic aneurysms (30, 31). Athero-

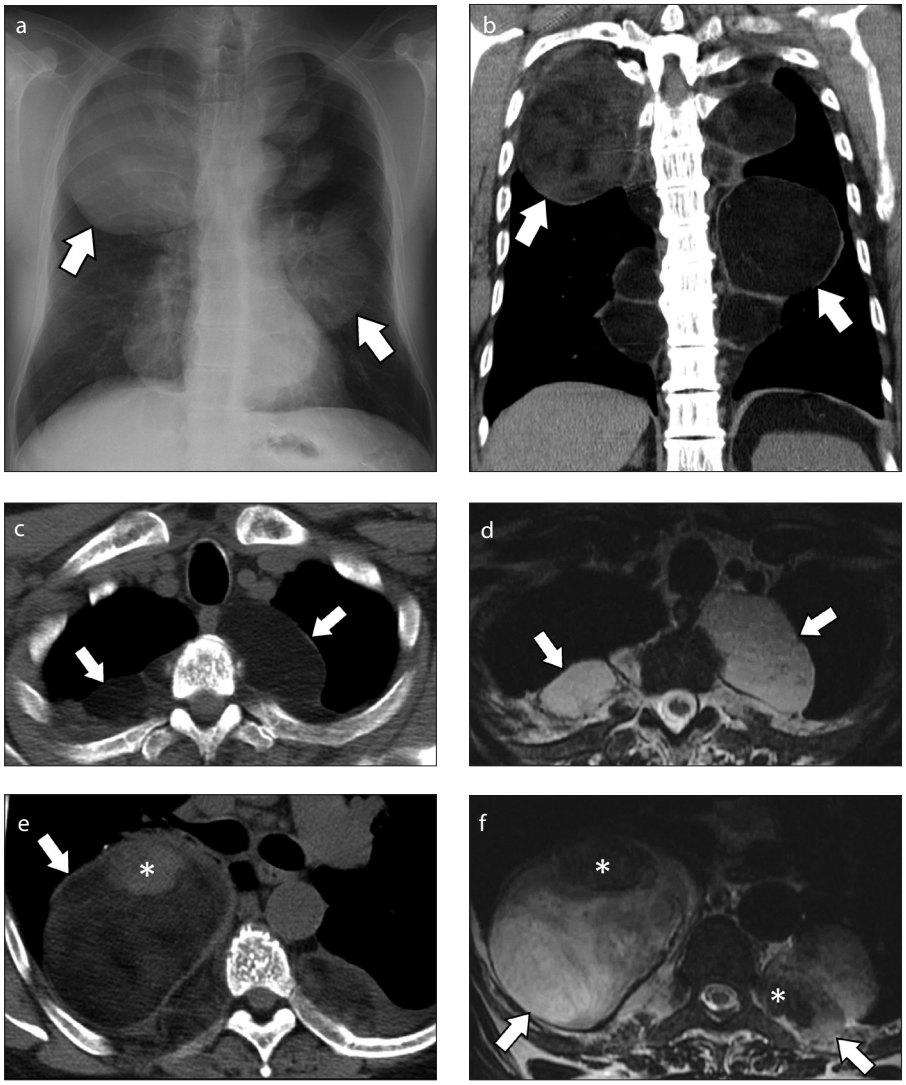

Figure 4. a–f. A 60-year-old male with extramedullary hematopoiesis, history of chronic anemia, and previous splenectomy. Posteroanterior CXR **(a)** shows multiple rounded opacities of various dimensions *(biggest ones indicated by arrows*) in both hemithoraces, without silhouetting heart and aorta. Coronal CT reformation image **(b)** confirms multiple masses *(biggest ones indicated by arrows),* with well-defined borders, along paravertebral areas. Axial unenhanced CT image **(c)** shows well-defined bilateral masses *(arrows)* with homogeneous fat attenuation in paraspinal areas at the level of T4. Fat attenuation values indicate inactivity of lesion. Axial T2-weighted MRI **(d)** at the same level as **(c)** shows bilateral masses *(arrows)* with signal intensity similar to mediastinal adipose tissue. Fatty deposition is consistent with inactivity of the the lesion. Axial unenhanced CT image **(e)** shows other bilateral paraspinal masses *(arrows)* at the level of T6 with higher attenuation values than the lesions shown in **(c)**. Note a soft-tissue rounded area *(asterisk)* in the non-dependent portion of the right mass. Axial T2-weighted image **(f)** at the same level as **(e)** shows areas with low signal intensity *(asterisks)* and areas with high signal intensity *(arrows)* due to fat deposition within the masses.

sclerosis is the most common etiology.

Most patients are asymptomatic, with the aneurysm found incidentally on imaging studies obtained for other indications. However, the acuity of symptomatic patients and the risks of surgical intervention make incidentally detected thoracic aneurysms clinically relevant. Therefore, the radiologist must be able to differentiate between "stable" lesions that only need follow-up (Fig. 5) and potentially "unstable" lesions that require prompt intervention. A thoracic aortic aneurysm is considered "unstable" when it is rapidly enlarging or shows signs of rupture or imminent rupture, such as a high-attenuation crescent within the aortic wall on unenhanced CT images, reflecting intramural hematoma. In addition, other findings of a rupture include focal discontinuity of intimal calcifications, eccentric shape of the aorta, and a "draped" aorta, which is defined as an indistinct margin of the posterior aortic wall from the adjacent vertebral body (32). Rupture of a descending aortic aneurysm usually occurs into the mediastinum and the left pleural space, producing periaortic soft-tissue hematoma, hemothorax, pleural or pericardial effusion, or even a contrast blush of active extravasation at the site of rupture (32, 33). The most relevant finding predictive of rupture is the maximum diameter of the aneurysm; a descending aorta aneurysm greater than 6–6.5 cm and enlarging more than 10–12 mm/year is a candidate for surgery (32, 33). Smaller aneurysms should be monitored annually, either by CT or MRI (32). Patients with renal impairment may benefit from sequences that do not require contrast administration, such as balanced steady-state free precession magnetic resonance angiography (33).

In the acute situation, CT or MRI are always required when CXR shows a widened mediastinum, displacement of the trachea to the right, enlargement of the aortic knob, or obliteration of the aortopulmonary window.

Endovascular treatment with stent implantation is becoming increasingly common for the treatment of "unstable" descending thoracic aortic aneurysm (32).

Aortic dissection

Dissection is the most common aortic emergency and has a poor prognosis (29, 34). It results from a tear in the intimal layer of aortic wall, allowing inflow of blood through the medial layer. This creates a "false lumen" that is separated from the "true lumen" by an intimal flap. According to the Stanford classification, dissections of the ascending aorta are categorized as type A and account for 62% of cases, whereas dissections of the descending aorta are categorized as type B and account for 38% of cases (32, 35). Type A dissections require urgent surgical repair, as they have a mortality rate over 50% within 48 hours if untreated (32, 34). Conversely, type B dissections are generally managed conservatively, with follow-up examinations every three to six months (35).

In 90% of cases, CXR shows such nonspecific abnormalities as abnormal cardiac contour, widening of the mediastinum, and displacement of aortic wall calcifications (34). Therefore, cross-sectional imaging plays a key role in the diagnosis of aortic dissection, which is essential for prompt and appropriate treatment (36).

Contrast-enhanced CT rapidly determines the type of dissection. It demonstrates the intimal flap in 70% of cases, and

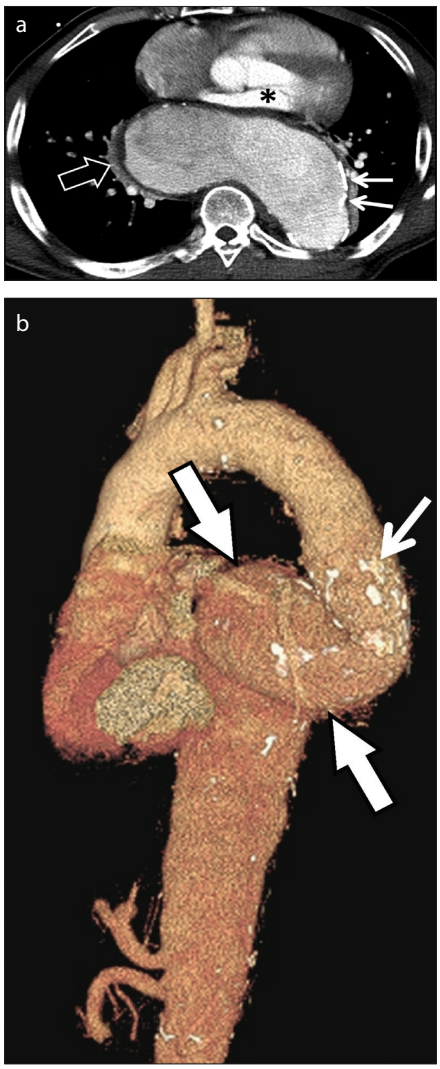

Figure 5. a, b. A 49-year-old man with "stable" aortic aneurysm. Axial contrast-enhanced CT scan **(a)** shows a large aneurysm of descending aorta with calcifications *(thin white arrows)* along the aortic wall. Large aneurysm causes passive atelectasis of the adjacent lung parenchyma *(black arrow)* and compression of the heart *(asterisk)*. Three-dimensional volume rendering image from lateral view **(b)** shows tortuosity of descending aorta and the extent of descending thoracic aorta aneurysm *(thick arrows)*, which continues into abdominal aorta. Note also calcifications *(thin arrow)* along the aortic wall.

Table 2. Clinical, histologic, and imaging characteristics useful in the differential diagnosis of foregut cysts

Characteristics	Neuroenteric cysts	Esophageal duplication cysts	Bronchogenic cysts
% of all mediastinal cysts	2–5	5–10	50–60
Most common age at presentation	By 1 year of life	Childhood	All ages
Foregut origin	Dorsal	Dorsal	Ventral
Histologic epithelium	Enteric and neural	Enteric	Respiratory
Most common location	Posterior mediastinum	Along esophagus, in lower right part of posterior mediastinum	Middle and posterior mediastinum
Most common clinical presentation	Pain, respiratory distress	Asymptomatic	Asymptomatic or cough, dyspnea, pain
CT findings helpful in differential diagnosis	Thin wall Communication with spinal canal	Thick wall Calcifications +	Thin wall Calcifications ++ Cartilage Air-fluid level (in superinfection)
Possible complications	-	Cyst rupture, hemorrhage	Infection, fistulization, malignant transformation
Associated malformations	Vertebral anomalies, bowel duplications, and mesenteric cysts	Malformations of gastrointestinal tract	-

CT, computed tomography; +, less common; ++, more common.

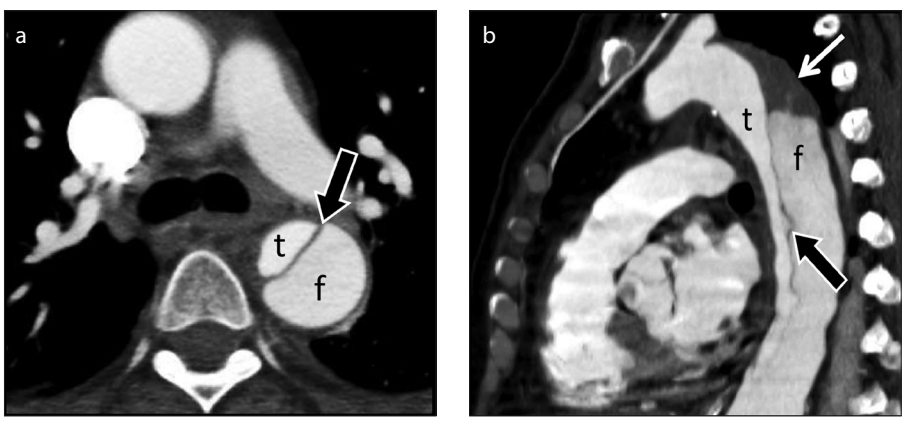

Figure 6. a, b. A 55-year-old woman with aortic dissection type B. Axial **(a)** and sagittal **(b)** contrast-enhanced CT images show intimal flap *(arrow)* in the descending aorta dividing true (t) and false (f) lumens and partial thrombosis of the false lumen *(white arrow)*.

the entry and re-entry points, signs of rupture, alteration of organ perfusion, dilation of the false lumen, and extension of the process into the aortic valve (32). Cardiac synchronization with electrocardiogram (ECG-gating) improves the evaluation of the aorta by reducing pulsatile artifacts, though this is most relevant in assessing the ascending aorta.

Recently, a "triple rule-out" CT protocol has been proposed as a new tool for simultaneously assessing three life-threatening causes of acute chest pain—aortic dissection, pulmonary embolism, and acute coronary syndrome. However, this protocol is not recommended if the clinical status is highly suspicious for aortic dissection (37).

MRI and transesophageal echocardiography are alternative imaging modalities. Nevertheless, the widespread availability of CT, as well as radiologist familiarity with the technique, makes this the modality of choice (33). If any imaging test is negative for aortic dissection, but a high clinical suspicion for dissection persists, testing with an alternative imaging modality is required (35).

Esophageal varices

Esophageal varices typically occur in the distal esophagus as a result of portal hypertension ("uphill varices") and bleed in one-third of cases, representing a life-threating complication in cirrhotic patients (38). Less commonly they can be caused by superior vena cava obstruction ("downhill varices")

and are usually located in the upper esophagus (39).

The reference standard for the diagnosis of esophageal varices is upper gastrointestinal endoscopy (27, 40). However, CT is a valuable tool for evaluating the cirrhotic liver and generally provides adequate coverage of the distal esophagus, where almost all varices develop (41). Thus, a single CT examination in cirrhotic patients can provide both liver imaging and varix evaluation. Both the positive and negative predictive values for the CT diagnosis of esophageal varices are high, ranging from 89% to 100% (40).

On CT, esophageal varices appear as thickening, intraluminal protrusions, or irregularities of the esophageal wall. Contrast material improves their detection, showing enhancing nodularities within the esophageal wall (4, 41). Dilated veins that are closely juxtaposed to the outer wall of the esophagus are called paraesophageal varices (Fig. 7), which are less prone to hemorrhage than varices located at the inner aspect of the esophageal lumen.

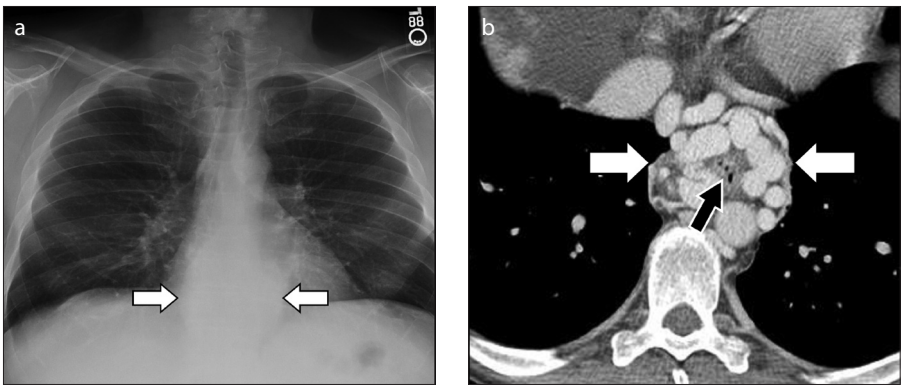

Figure 7. a, b. A 48-year-old man with esophageal varices and cirrhosis. Posteroanterior CXR **(a)** shows widening of the inferior third of the azygoesophageal recess *(arrows)*. Axial enhanced CT scan obtained in venous phase **(b)** shows multiple enlarged venous vessels *(white arrows)* closely juxtaposed to the outer wall of the esophagus *(black arrow)*, consistent with paraesophageal varices.

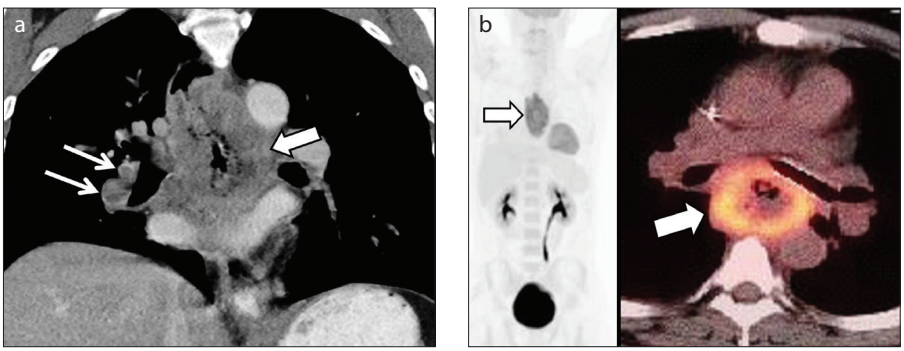

Figure 8. a, b. A 59-year-old man with squamous cell carcinoma of the esophagus. Coronal reformation CT image at mediastinal window setting **(a)** shows craniocaudal extent of the mass *(thick arrow)* in the middle third of the esophagus, with heterogeneous contrast enhancement. Pulmonary embolism of interlobar artery can also be seen *(thin arrows)*. 18F-FDG-PET/CT scan **(b)** shows increased tracer uptake in the esophageal tumor *(arrows)* without any additional area of hypermetabolism.

Dilated azygos vein

A dilated azygos vein may result from overhydration and pregnancy, as well as from such pathologic causes as congestive heart failure, portal thrombosis, obstruction of the superior or inferior vena cava, congenital interrupted inferior vena cava with azygos (or hemiazygos) continuation, and azygos vein aneurysm (42, 43).

CXR shows a widened right paraspinal line, which is proved to represent a dilated azygos vein by CT or MRI demonstration of typical enhancement in the venous phase. Cross-sectional imaging modalities can also show atretic segments or complete absence of the inferior vena cava if there is an interrupted inferior vena cava with azygos continuation (44).

Esophagus

Esophageal neoplasms

Esophageal neoplasms can be malignant (80%) or benign (20%) (45). Malignant esophageal neoplasms are mainly squamous cell carcinoma and adenocarcinoma (45).

In the work-up of a malignant esophageal neoplasm, CXR and esophagography have been largely replaced by endoscopy (46). Endoscopy allows the evaluation of even small esophageal lesions and permits tissue sampling of both the esophageal wall and regional lymph nodes. Endoscopic ultrasound combined with fine-needle aspiration (EUS-FNA) helps in the assessment of regional lymph nodes, though it is limited to those located less than 2 cm from the esophageal lumen (46).

Once the histologic diagnosis is confirmed, CT of the chest and abdomen is recommended for assessing local and distant spread of disease (46). Oral and intravenous contrast material should be used to improve visualization of the esophageal lumen and mediastinal structures (46). In early stages, CT can show a soft-tissue mass or a focal thickening of the esophageal wall, which progresses to diffuse circumferential involvement in more advanced stages (Fig. 8). Most squamous cell carcinomas are located in the middle third of the esophagus, whereas adenocarcinomas are located in the lower third because they almost always arise from a preexisting Barrett's esophagus (45). Nodal staging is the main limitation of CT, as size is not a reliable predictor of malignancy in these tumors (47).

MRI does not substantially improve nodal staging, and its overall diagnostic performance does not exceed the above mentioned techniques (46, 48). Malignant esophageal tumors usually produce intermediate signal intensity on T2-weighted images, unless they contain a high amount of extracellular mucin, which characteristically turns them hyperintense on these sequences (45).

^{18}F-FDG-PET scanning is recommended to improve the accuracy of staging of distant disease in patients who are potential candidates for curative therapy, whereas the value of ^{18}F-FDG-PET as a predictive marker of response to neoadjuvant therapy remains uncertain (Fig. 8) (49, 50).

Benign esophageal neoplasms include a wide variety of histologic types, mainly represented by leiomyomas. Fibrovascular polyps are important for their clinical presentation, with sudden death from asphyxia reported when they are regurgitated into the mouth.

On CT, a leiomyoma appears as a homogeneous mass in the mid to lower esophagus, whereas a fibrovascular polyp is a heterogeneous mass of fibrous and fat tissue located

in the cervical esophagus and extending into the distal esophagus (Fig. 9) (45). ^{18}F-FDG-PET is usually negative in patients with benign tumors, due to their low growth rate (45).

Esophageal duplication cyst

Esophageal duplication cysts account for 5%–10% of all foregut cysts (3). They are commonly asymptomatic in both children and adults, but occasionally present with symptoms of airway or esophageal compression (37). Hemorrhage and cyst rupture are complications that may occur if the lesion contains gastric or pancreatic tissue (11).

On CXR, esophageal cysts appear as solitary, rounded, well-defined mediastinal lesions, similar to other foregut cysts (8). On CT they appear as single homogeneous mass with regular and well-defined borders (Fig. 10) and low-to-high attenuation values, due to their fluid or proteinaceous content, respectively (25, 26). They are located in the lower right part of the posterior mediastinum within the esophageal wall or closely adjacent to it (3, 51). A thick wall and calcification may help in distinguishing an esophageal duplications cyst from other foregut cysts (Table 2) (3, 25). On MRI, esophageal duplication cysts have high signal intensity on T2-weighted images (Fig. 10) and usually are of low signal intensity on T1-weighted sequences (12). Contrast administration is recommended on both CT and MRI, as the complete absence of enhancement within the cyst is characteristic of benignity (Fig. 10) (25).

^{99m}Technetium-pertechnetate scan can help in identifying esophageal cysts containing ectopic gastric mucosa, which are at higher risk of developing cyst rupture and hemorrhage (51). Endoscopy can detect esophageal cysts, though endoscopic biopsies should be avoided as they may complicate subsequent surgical excision (51).

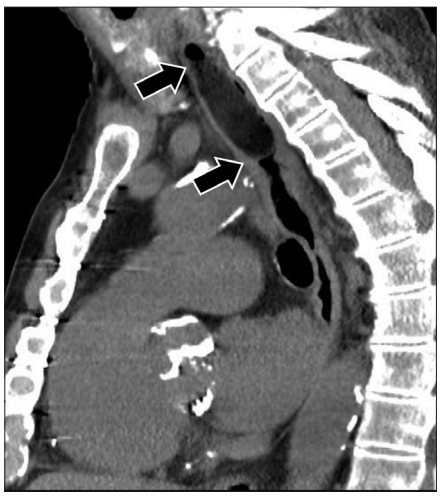

Figure 9. A 90-year-old man with fibrovascular polyp. Unenhanced sagittal CT image shows a 6 cm mass *(between arrows)* of fat attenuation within the upper thoracic esophagus.

Lymph nodes

Lymphoma

Patients with primary mediastinal lymphoma typically have an anterior mediastinal mass often associated with enlarged nodes in the middle and posterior mediastinum (52). Rarely, lymphoma can appear as a solitary homogeneous mass in the paravertebral area, difficult to distinguish from a neurogenic tumor (Fig. 11) (53). On CT, enlarged lymph nodes usually have homogeneous soft-tissue attenuation with mild-to-moderate contrast enhancement. If large, however, they can show cystic or necrotic changes (54). CT can depict the anatomic extent of disease and also allow an evaluation of abdominal lymph nodes (8). Therefore, MRI is not commonly used in evaluating lymphoma. If performed, lymphoma appears as one or more, relatively homogeneous masses with low signal intensity on T1-weighted images and intermediate-to-high signal on T2-weighted images (3). MRI can also evaluate treatment response after chemotherapy, showing inactive residual fibrotic masses as homogeneous, hypointense, and nonenhancing lesions (54). To obtain a global evaluation, ^{18}F-FDG-PET scanning is recommended 6–8 weeks after treatment in patients with Hodgkin's lymphoma and diffuse large B-cell lymphoma, which are FDG-avid and potentially curable (55).

Lymphadenopathy

Lymph node metastases in the posterior mediastinum can develop with both intra- and extrathoracic tumors (12). The only widely accepted criterion suggestive of malignancy is a short-axis node diameter greater than 10 mm (56, 57). However, this approach may result in both false positives and false negatives, due to inflammatory nodal enlargement and the presence of metastases in normal-sized lymph nodes, respectively.

Posterior mediastinal lymph nodes can also be involved in inflammatory disorders, such as sarcoidosis, lymphangioleiomyomatosis, and amyloidosis, as well as infections, most commonly HIV, Mycobacterium tuberculosis, and Mycobacterium

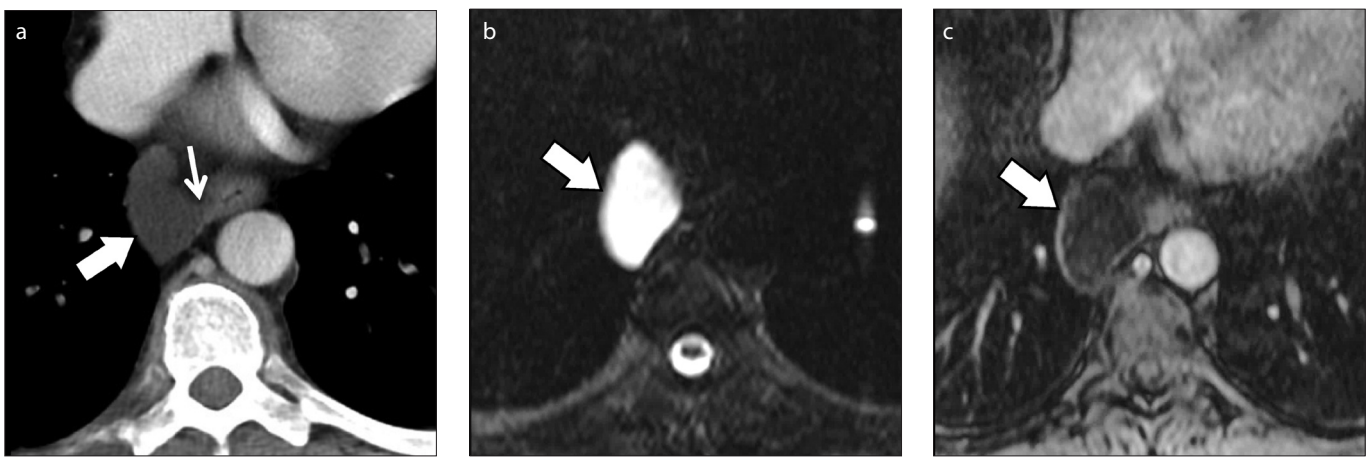

Figure 10. a–c. A 50-year-old woman with esophageal duplication cyst. Axial enhanced CT image **(a)** shows a homogeneous mass *(thick arrow)* of water attenuation with well-defined borders, located in the lower right part of posterior mediastinum, closely adjacent to the esophageal wall *(thin arrow)*. Axial T2-weighted half-Fourier acquisition single-shot turbo spin-echo MRI **(b)** demonstrates high signal intensity within the lesion *(arrow)*, compatible with serous content. Axial T1-weighted image after contrast administration **(c)** shows complete absence of enhancement within the cyst *(arrow)*, a characteristic of benignity.

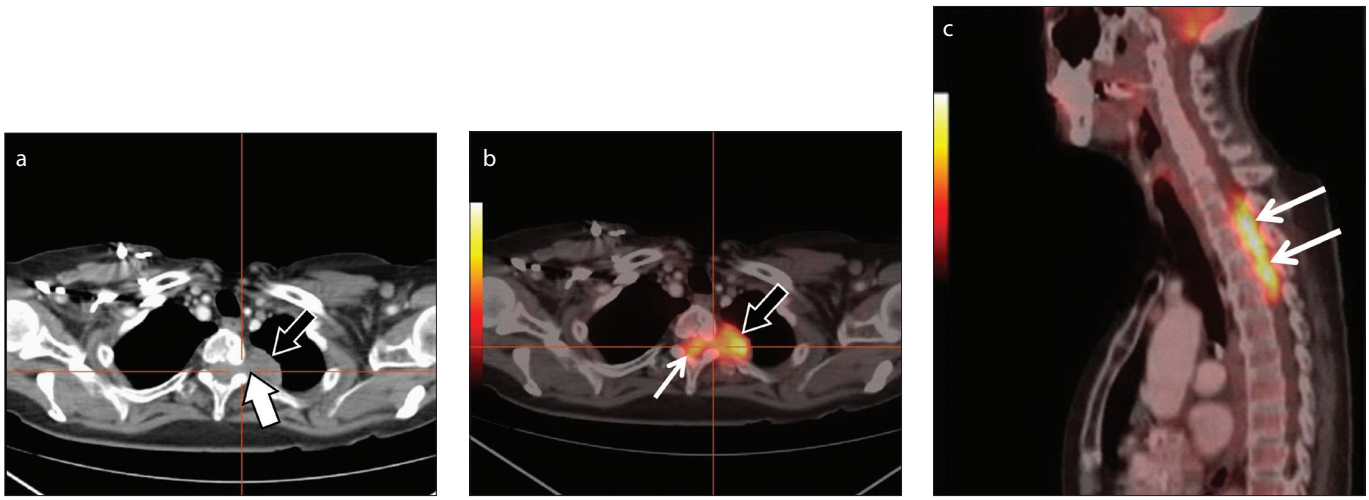

Figure 11. a–c. A 60-year-old man with diffuse large B-cell lymphoma. Axial enhanced CT scan image **(a)** shows a soft-tissue mass *(black arrow)* in the paravertebral area, with smooth and regular margins towards the left lung parenchyma. Mass extends into the spinal canal through the widened intervertebral canal *(white arrow)*. Axial **(b)** and sagittal **(c)** 18FDG-PET/CT fusion images show intense FDG uptake in the mass *(black arrow)* and in the vertebral canal *(thin arrows)*, consistent with invasion of the vertebral canal.

avium complex. Enlarged lymph nodes with low-attenuation values are more common in mycobacterial infection and lymphangioleiomyomatosis (4). However, imaging features are not specific and must be combined with clinical presentation and laboratory tests in the diagnostic work-up. EUS-FNA helps in obtaining a definitive diagnosis of posterior mediastinal nodes, with an accuracy in detecting metastases ranging from 83% to 98% (58).

Adipose tissue

Lipoma and liposarcoma

Lipoma and especially liposarcoma are fat-containing tumors that can arise from the adipose tissue of posterior mediastinum or can be an intrathoracic extension of a retroperitoneal lipoma or liposarcoma (9, 12). Because of their slow growth, lipomas and liposarcomas of the posterior mediastinum are usually large at presentation (12). On CXR, these fatty tumors present as large opacities, which prompt further diagnostic evaluation by CT or MRI (Fig. 12). On CT, lipomas appear as homogeneous fatty masses with well-defined margins and attenuation values ranging between -30 and -100 HU (4). Conversely, liposarcomas are heterogeneous (Fig. 12), with a mean attenuation value greater than -30 HU, due to soft tissue and fibrous bands alternating with areas of fat (4, 59). Attenuation values can even be similar to solid tumors in cases of poorly differentiated liposarcomas, which are more cellular and contain less fat.

On MRI, lipomas appear as well-defined, avascular, homogeneous masses with signal intensity typical of fat tissue—hyperintense on both T1- and T2-weighted images, with uniform signal loss on fat-suppressed images (60). Conversely, liposarcomas present as heterogeneous masses with various amounts of soft tissue and have heterogeneous contrast enhancement (59, 61).

On ^{18}F-FDG-PET scanning, liposarcomas usually show higher FDG uptake than lipomas. However, there may be false negatives with low-grade liposarcomas and false positives with brown fat deposits (61).

Differential diagnosis includes mediastinal lipomatosis (Fig. 13), a benign condition characterized by excessive deposition of mature adipose tissue within the mediastinum. Compression of adjacent structures is rare (62, 63).

Diaphragm

Hiatal hernia

Hiatal hernia refers to the herniation of elements of the abdominal cavity into the chest. There are two main types of hiatal hernias: sliding and paraesophageal. In a sliding hernia, the gastroesophageal junction migrates above the diaphragm through the esophageal hiatus, whereas in a paraesophageal hernia, the stomach herniates without any displacement of the gastroesophageal junction. Sliding hernias, which account for more than 95% of cases, are often associated with gastroesophageal reflux disease (64, 65). Conversely, paraesophageal hernias may present acutely with obstructive symptoms due to gastric volvulus, which may cause bleeding, incarceration, strangulation, and perforation of the stomach and intestine (64). The most recent guidelines suggest surgical repair of all symptomatic paraesophageal hernias and preventive repair of asymptomatic paraesophageal hernias only after a careful evaluation of patient and comorbidities (64).

CXR may depict larger hiatal hernias as an opacity in the posterior mediastinum, often containing air or an air-fluid level (Fig. 14). On the frontal view, it causes widening of the inferior third of the azygoesophageal recess and can produce a double contour behind the cardiac silhouette. However, smaller hernias may remain invisible on CXR, and their detection may require an esophagram or upper gastrointestinal endoscopy.

CT is superior to CXR for delineating gastric herniation through the esophageal hiatus, which is usually accompanied by the herniation of a variable amount of low-attenuation fat (Fig. 14) and by paraesophageal fluid collections in patients with ascites (66). However, some hiatal hernias cannot be detected on CT because they can slide back into the abdomen in the supine position.

MRI and nuclear medicine studies are not routinely used in the diagnosis of hiatal hernia, as they offer no advantages over esophagram and CT (64).

Bochdalek hernia

In a Bochdalek hernia, abdominal fat or viscera herniate into the thorax through a defect in the posteromedial portion of the diaphragm. Most larger and symptomatic hernias are diagnosed during the neonatal

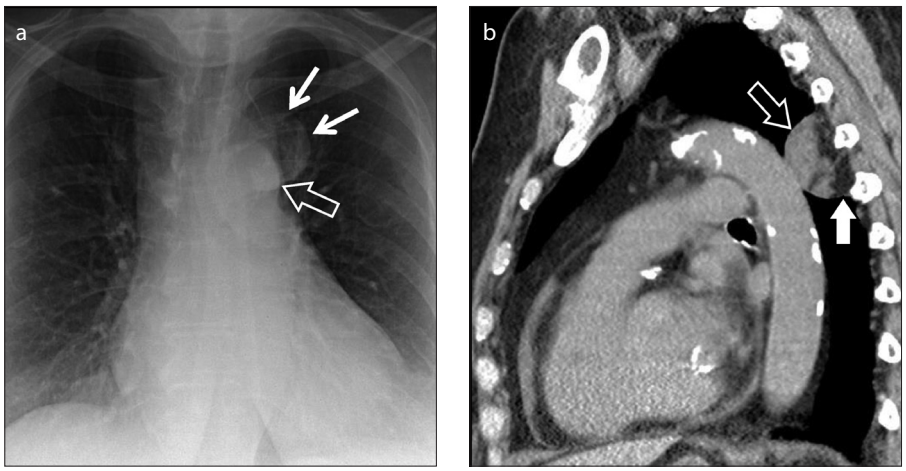

Figure 12. a, b. A 76-year-old woman with liposarcoma. Posteroanterior CXR **(a)** shows rounded opacity *(white arrows)* with smooth borders superimposed on aortic knob *(open arrow)*, without producing a "silhouette sign" with the aorta. Lack of the "silhouette sign" implies that the lesion is anterior or posterior to the aorta. Sagittal CT reformation **(b)** shows a heterogeneous posterior mediastinal mass containing areas of fat *(white arrow)* and soft-tissue attenuation *(black arrow)*.

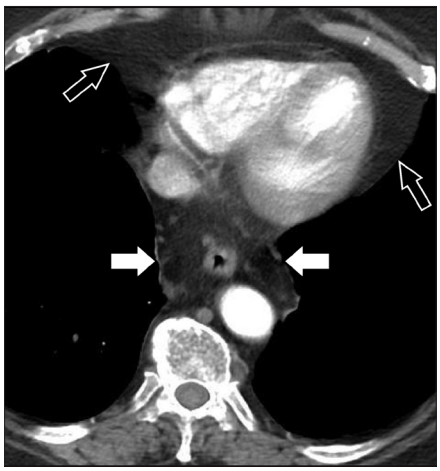

Figure 13. An 81-year-old woman with mediastinal lipomatosis. Axial CT image demonstrates excess fat deposition in the lower posterior mediastinum (white arrows) around the esophagus without compression. Note prominent fat in cardiophrenic angles *(black arrows)*, consistent with epicardial fat pads.

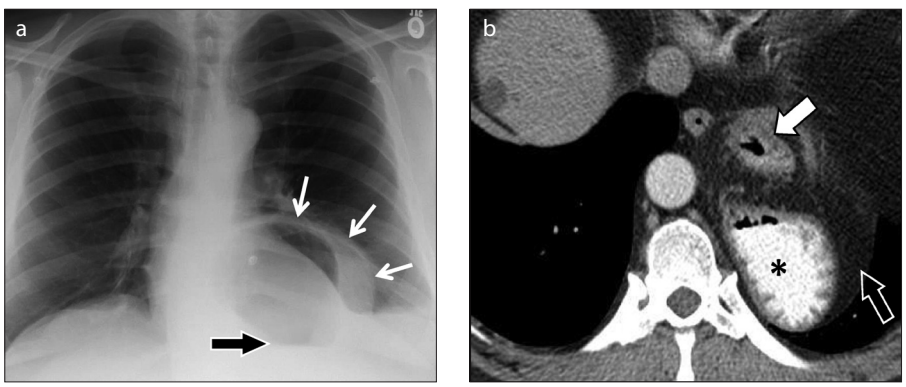

Figure 14. a, b. A 51-year-old man with acute abdominal pain and paraesophageal hernia. Posteroanterior CXR **(a)** shows large opacity *(white arrows)* with inner air-fluid level *(black arrow)*. Enhanced axial CT image after oral contrast administration **(b)** shows herniation of part of the stomach *(asterisk)* and abdominal adipose tissue *(black arrow)* through esophageal hiatus. Note separation between the esophagus *(white arrow)* and stomach *(asterisk)*.

period, because the herniation of abdominal organs causes severe respiratory distress. However, asymptomatic Bochdalek hernias can be incidentally found in 10.5% of adults undergoing chest or abdominal CT examinations (67).

CXR may fail to show the herniation, whereas CT and MRI allow accurate detection and characterization of Bochdalek hernia and such potential complications as bowel incarceration, strangulation, or perforation (68, 69).

On CT and MRI, a Bochdalek hernia typically appears as a discontinuity of the diaphragmatic musculature adjacent to a fatty homogeneous mass that abuts the thoracic surface of the diaphragm (Fig. 15) (69). In addition to fat, abdominal organs can pass through the diaphragmatic tear, including bowel, omentum, spleen, left lobe of the liver, stomach, kidney and pancreas on the left, and part of the liver and kidney on the right (70). Multiplanar CT and MRI images are useful for showing the diaphragmatic defect (Fig. 15) and the contents of the hernia sac (67, 71). This defect is the key finding for differentiating a Bochdalek hernia from diaphragmatic eventration or a diaphragmatic lipoma or liposarcoma (68).

Extrathoracic lesions extending into the mediastinum

Intrathoracic goiter

A goiter is defined as "intrathoracic" when the bulk of its mass is located below the thoracic inlet. One-fourth of all intrathoracic goiters involve the posterior mediastinum, especially in patients with a previous history of thyroid surgery (4, 72). Posterior mediastinal goiters occur exclusively on the right, because the left brachiocephalic vein and the aortic arch on the left represent a natural anatomical barrier (4).

On CXR, a posterior mediastinal goiter presents as a paratracheal or retrotracheal opacity. On the posteroanterior view, it has sharp and well-defined margins with the lung parenchyma above and below the level of the right clavicle, indicating its location in the posterior mediastinum ("cervicothoracic sign") (Fig. 16) (73).

Barium swallow may identify esophageal compression from a mediastinal goiter as the cause of dysphagia. However, CT is the imaging modality of choice for assessing the extent of a posterior mediastinal goiter (Fig. 16). It appears as a mass with well-defined margins, lobulated borders, focal calcifications, and usually high attenuation value on unenhanced images because of its intrinsic iodine content (26, 74). After contrast administration, the goiter shows intense, sustained, and heterogeneous enhancement, due to degenerative cystic areas of low-attenuation within the lesion (Fig. 16) (4). Although the anatomic continuity of the goiter with the cervical thyroid is diagnostic of intrathoracic extension of the thyroid gland, absence of this finding does not exclude a mediastinal goiter, since the connection may be narrow, fibrous, or a vascular pedicle (4).

CT and radionuclide scintigraphy with ^{123}iodine or ^{99m}Tc-pertechnetate are sufficient to make the diagnosis (11, 75). However, scintigraphy may overlook those goiters with hemorrhage and cystic degeneration, and iodinated contrast material during a CT scan in a patient with thyroid dysfunction may exacerbate thyrotoxicosis. Thus, MRI can be helpful, showing the goiter as a mass with heterogeneous high signal intensity on T2-weighted images, due to the presence of hemorrhage, necrosis, cysts, and calcification.

An intrathoracic goiter is an indication for surgery even in asymptomatic patients, since it may develop pressure effects and malignancy. CT assessment is essential in surgical planning, as intrathoracic goiters located in the posterior mediastinum require a lateral thoracotomy instead of a cervical approach (76).

Pancreatic pseudocyst

A pancreatic pseudocyst is a collection of pancreatic secretions without necrosis, enclosed by a well-defined wall of fibrous or granulation tissue, which develops four or more weeks after the clinical onset of pancreatitis (77). A pancreatic pseudocyst develops adjacent to the pancreas, though it may also extend into the mediastinum. The migration of pancreatic secretions and inflammatory products occurs most commonly through the esophageal or aortic hiatus. Therefore, the posterior mediastinum is the most common location (78).

CXR shows widening of the mediastinum or a retrocardiac opacity, often associated with pleural effusion. Contrast CT is the imaging study of choice, because it shows the connection between the mediastinal mass and an abdominal pancreatic pseudocyst. The mediastinal mass has a well-defined enhancing wall and fluid-attenuation values. If this connection cannot be identified on CT, magnetic resonance cholangiopancreatography can be helpful. When imaging cannot reveal this connection, EUS-guided aspiration of the cyst demonstrating of a high amylase level is diagnostic (78).

Imaging is also crucial for identifying complications, including infection of the cyst, hemorrhage, fistulization, rupture, and mediastinitis. Pleural effusions develop in 50% of cases (78). A thick and irregular wall is a sign of an infected pseudocyst, while higher attenuation values reflect intracystic hemorrhage (4, 79).

Large pseudocysts may require endoscopic drainage, CT-guided percutaneous drainage, or even surgery in case of complications (78).

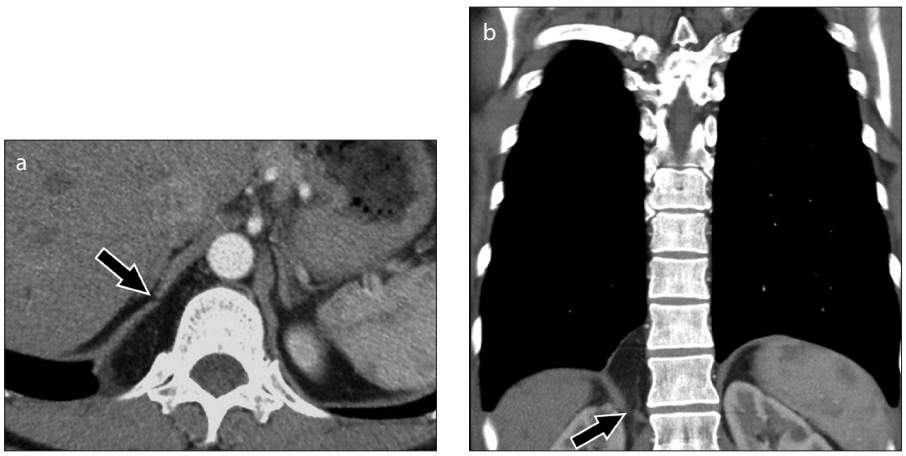

Figure 15. a, b. A 48-year-old man with Bochdalek hernia. Axial **(a)** and coronal reformation **(b)** CT images show herniation of abdominal fat through discontinuity of the medial portion of the diaphragm *(arrows)*.

Conclusion

A wide variety of disorders can arise from the anatomical structures of the posterior mediastinum. Each imaging modality plays a fundamental role in the detection and characterization of these disorders, an-

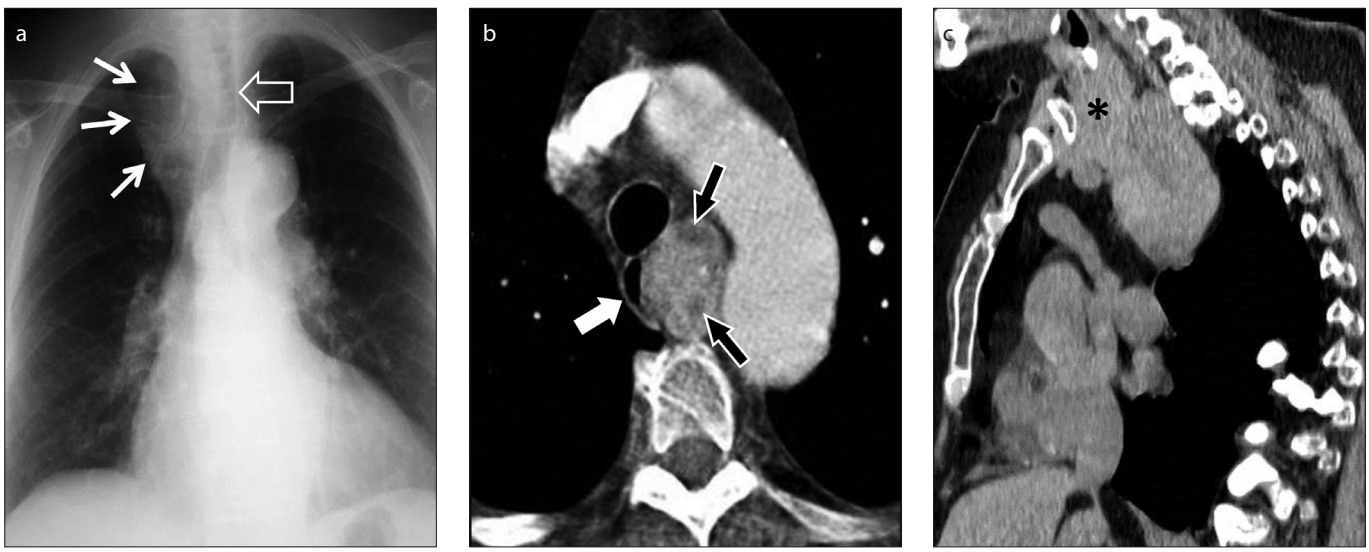

Figure 16. a–c. Intrathoracic goiter in a 60-year-old woman. Posteroanterior CXR **(a)** shows opacity *(thin arrows)* above the level of the right clavicle, with sharp and well-defined margins ("cervicothoracic sign") due to its location in posterior mediastinum. The mass produces left displacement of the trachea *(open arrow)*. Axial **(b)** and sagittal **(c)** enhanced CT images show a heterogeneous soft-tissue mass with hypodense areas *(black arrows)* due to cystic degeneration in the posterior mediastinum. Goiter causes compression and rightward displacement of the esophagus *(white arrow)*. The mass extends from the cervical region as a continuation of the thyroid gland *(asterisk)*.

Table 3. Preferential imaging modality for specific diagnostic questions on posterior mediastinal lesions

Posterior mediastinal lesions	Questions answered by CT	Questions answered by MRI
Neurogenic tumors	- Is there erosion or scalloping of ribs or vertebrae? - Are there distant metastases in bones, lung, or liver?	- Does the tumor have a "salt-and- pepper", "whorled", or "target" appearance? - Is there extension into the spinal canal or invasion of nerve roots?
Infectious spondylitis	- Is the intervertebral disc hypodense or completely destroyed? - Are there any calcifications?	- Is there involvement of the epidural space? - Does the lesion compress the spinal cord and nerve roots?
Extramedullary hematopoiesis	N/A	- Does the lesion compress the spinal cord and nerve roots?
Meningocele	- Are there vertebral abnormalities? - Is the intervertebral foramen enlarged?	- Is there a connection to the spinal canal?
Neuroenteric cyst	- Are there vertebral abnormalities like hemivertebrae, butterfly vertebrae, scoliosis, anterior spina bifida, or split notochord syndrome?	- Is there a connection to or extension into the spinal canal?
Thoracic aortic aneurysm	- Are the calcifications discontinuous?	N/A
Aortic dissection	- Is there aortic dissection in this instable patient?	N/A
Esophageal varices	- Are varices localized in the inner or outer aspect of esophageal lumen (i.e., esophageal or paraesophageal)?	N/A
Dilated azygos vein	- Is it secondary to portal thrombosis or obstruction of the superior or inferior vena cava?	N/A
Esophageal neoplasms	- Are there distant metastases in lung, bones, liver?	N/A
Esophageal duplication cyst	- Are there calcifications?	N/A
Lymphoma	- Is it localized or does it involve other mediastinal structures or distant organs?	- After a therapy, is the mass still a viable tumor or only residual fibrosis?
Lymphadenopathy	- Is there any sign of intra- or extrathoracic tumor or inflammatory disease?	N/A
Hiatal hernia	- Is the hernia complicated by a gastric volvulus, with bleeding, incarceration, strangulation, and perforation?	N/A
Bochdalek hernia	- Is the hernia complicated by bowel incarceration, strangulation, or perforation?	N/A
Intrathoracic goiter	- Does the mass have a high attenuation value on the unenhanced scan? - Are there calcifications?	N/A
Pancreatic pseudocyst	- Is it complicated by pleural effusions, infection, hemorrhage, fistulization, rupture, or mediastinitis?	N/A

N/A, not applicable.

swering different morphologic questions to provide definite diagnostic information as summarized in Table 3.

Acknowledgements

We thank Dr. Lorenzo Bonomo, Department of Radiological Sciences, Catholic University of Sacred Heart, Policlinico Universitario "A. Gemelli", Rome, Italy; Dr. José Vilar, Hospital Universitario "Dr Peset", Valencia, Spain; and Dr. Carles Lorenzo Bosquet, Hospital Universitario "Vall d'Hebron", Barcelona, Spain, for their valuable contributions to this review.

Conflict of interest disclosure

Alexander A. Bankier is a consultant for Spiration (Olympus Medical Systems) and has received authorship honoraria from Elsevier.

Elisa Franquet is founded by "Fundación Alfonso Martín Escudero", Avenida de Brasil 30, 28020 Madrid, Spain.

References

1. Zylak CJ. Diagnostic approach to radiology of the mediastinum. In: Taveras LM, Ferrucci JT, eds. Radiology: diagnosis-imaging-intervention. Philadelphia: Lippincott, 1986.
2. Reeder LB. Neurogenic tumors of the mediastinum. Semin Thorac Cardiovasc Surg 2000; 12:261–267. [CrossRef]
3. Strollo DC, Rosado-de-Christenson ML, Jett JR. Primary mediastinal tumors: part II. Tumors of the middle and posterior mediastinum. Chest 1997; 112:1344–1357. [CrossRef]
4. Kawashima A, Fishman EK, Kuhlman JE, Nixon MS. CT of posterior mediastinal masses. Radiographics 1991; 11:1045–1067. [CrossRef]
5. Balcombe J, Torigian DA, Kim W, Miller WT, Jr. Cross-sectional imaging of paragangliomas of the aortic body and other thoracic branchiomeric paraganglia. AJR Am J Roentgenol 2007; 188:1054–1058. [CrossRef]
6. Guan YB, Zhang WD, Zeng QS, Chen GQ, He JX. CT and MRI findings of thoracic ganglioneuroma. Br J Radiol 2012; 85:e365–372. [CrossRef]
7. Duffy S, Jhaveri M, Scudierre J, Cochran E, Huckman M. MR imaging of a posterior mediastinal ganglioneuroma: fat as a useful diagnostic sign. AJNR Am J Neuroradiol 2005; 26:2658–2662.
8. Ranganath SH, Lee EY, Restrepo R, Eisenberg RL. Mediastinal masses in children. AJR Am J Roentgenol 2012; 198:W197–216. [CrossRef]
9. Juanpere S, Cañete N, Ortuño P, Martínez S, Sanchez G, Bernado L. A diagnostic approach to the mediastinal masses. Insights Imaging 2013; 4:29–52. [CrossRef]
10. Zhang Y, Nishimura H, Kato S, et al. MRI of ganglioneuroma: histologic correlation study. J Comput Assist Tomogr 2001; 25:617–623. [CrossRef]
11. Duwe BV, Sterman DH, Musani AI. Tumors of the mediastinum. Chest 2005; 128:2893–2909. [CrossRef]
12. Restrepo CS, Eraso A, Ocazionez D, Lemos J, Martinez S, Lemos DF. The diaphragmatic crura and retrocrural space: normal imaging appearance, variants, and pathologic conditions. Radiographics 2008; 28:1289–1305. [CrossRef]
13. Baleriaux DL, Neugroschl C. Spinal and spinal cord infection. Eur Radiol 2004; 14 (Suppl 3):E72–83.
14. Harisinghani MG, McLoud TC, Shepard JA, Ko JP, Shroff MM, Mueller PR. Tuberculosis from head to toe. Radiographics 2000; 20:449–470. [CrossRef]
15. Le Page L, Feydy A, Rillardon L, et al. Spinal tuberculosis: a longitudinal study with clinical, laboratory, and imaging outcomes. Semin Arthritis Rheum 2006; 36:124–129. [CrossRef]

16. Oztekin O, Calli C, Adibelli Z, Kitis O, Eren C, Altinok T. Brucellar spondylodiscitis: magnetic resonance imaging features with conventional sequences and diffusion-weighted imaging. Radiol Med 2010; 115:794–803. [CrossRef]
17. Staatz G, Adam GB, Keulers P, Vorwerk D, Gunther RW. Spondylodiskitic abscesses: CT-guided percutaneous catheter drainage. Radiology 1998; 208:363–367. [CrossRef]
18. Ginzel AW, Kransdorf MJ, Peterson JJ, Garner HW, Murphey MD. Mass-like extramedullary hematopoiesis: imaging features. Skeletal Radiol 2012; 41:911–916. [CrossRef]
19. Haidar R, Mhaidli H, Taher AT. Paraspinal extramedullary hematopoiesis in patients with thalassemia intermedia. Eur Spine J 2010; 19:871–878. [CrossRef]
20. Haran M, Ni S. Recurrent reversible paraplegia. The Lancet 2001; 357:1092. [CrossRef]
21. Tsitouridis J, Stamos S, Hassapopoulou E, Tsitouridis K, Nikolopoulos P. Extramedullary paraspinal hematopoiesis in thalassemia: CT and MRI evaluation. Eur J Radiol 1999; 30:33–38. [CrossRef]
22. Sohawon D, Lau KK, Lau T, Bowden DK. Extra-medullary haematopoiesis: a pictorial review of its typical and atypical locations. J Med Imaging Radiat Oncol 2012; 56:538–544. [CrossRef]
23. Georgiades CS. Neyman EG, Francis IR, Sneider MB, Fishman EK. Typical and atypical presentations of extramedullary hemopoiesis. AJR Am J Roentgenol 2002; 179:1239–1243. [CrossRef]
24. Rainov NG, Heidecke V, Burkert W. Thoracic and lumbar meningocele in neurofibromatosis type 1. Report of two cases and review of the literature. Neurosurg Rev 1995; 18:127–134. [CrossRef]
25. Jeung MY, Gasser B, Gangi A, et al. Imaging of cystic masses of the mediastinum. Radiographics 2002; 22:S79–93. [CrossRef]
26. Laurent F, Latrabe V, Lecesne R, et al. Mediastinal masses: diagnostic approach. Eur Radiol 1998; 8:1148–1159. [CrossRef]
27. Garcia-Tsao G, Sanyal AJ, Grace ND, Carey W. Prevention and management of gastroesophageal varices and variceal hemorrhage in cirrhosis. Hepatology 2007; 46:922–938. [CrossRef]
28. Reed JC, Sobonya RE. Morphologic analysis of foregut cysts in the thorax. AJR Am J Roentgenol 1974; 120:851–860. [CrossRef]
29. Hiratzka LF, Bakris GL, Beckman JA, et al. 2010 ACCF/AHA/AATS/ACR/ASA/SCA/SCAI/SIR/STS/SVM guidelines for the diagnosis and management of patients with thoracic aortic disease: a report of the American College of Cardiology Foundation/American Heart Association Task Force on Practice Guidelines, American Association for Thoracic Surgery, American College of Radiology, American Stroke Association, Society of Cardiovascular Anesthesiologists, Society for Cardiovascular Angiography and Interventions, Society of Interventional Radiology, Society of Thoracic Surgeons, and Society for Vascular Medicine. Circulation 2010; 121:e266–369. [CrossRef]
30. Bickerstaff LK, Pairolero PC, Hollier LH, et al. Thoracic aortic aneurysms: a population-based study. Surgery 1982; 92:1103–1108.
31. Clouse W, Hallett, Jr JW, et al. Improved prognosis of thoracic aortic aneurysms: A population-based study. JAMA 1998; 280:1926–1929. [CrossRef]
32. Chiu KW, Lakshminarayan R, Ettles DF. Acute aortic syndrome: CT findings. Clin Radiol 2013; 68:741–748. [CrossRef]
33. Holloway BJ, Rosewarne D, Jones RG. Imaging of thoracic aortic disease. Br J Radiol 2011; 84:S338–354. [CrossRef]
34. McMahon MA, Squirrell CA. Multidetector CT of aortic dissection: a pictorial review. Radiographics 2010; 30:445–460. [CrossRef]
35. Upadhye S, Schiff K. Acute aortic dissection in the emergency department: diagnostic challenges and evidence-based management. Emerg Med Clin North Am 2012; 30:307–327. [CrossRef]
36. Booher AM, Eagle KA. Diagnosis and management issues in thoracic aortic aneurysm. Am Heart J 2011; 162:38–46. [CrossRef]
37. Ayaram D, Bellolio MF, Murad MH, et al. Triple rule-out computed tomographic angiography for chest pain: a diagnostic systematic review and meta-analysis. Acad Emerg Med 2013; 20:861–871. [CrossRef]
38. Toubia N, Sanyal AJ. Portal hypertension and variceal hemorrhage. Med Clin North Am 2008; 92:551–574. [CrossRef]
39. Felson B, Lessure AP. "Downhill" varices of the esophagus. Dis Chest 1964; 46:740–746. [CrossRef]
40. Lipp MJ, Broder A, Hudesman D, et al. Detection of esophageal varices using CT and MRI. Dig Dis Sci 2011; 56:2696–2700. [CrossRef]
41. Kim YJ, Raman SS, Yu NC, To'o KJ, Jutabha R, Lu DSK. Esophageal varices in cirrhotic patients: evaluation with liver CT. AJR Am J Roentgenol 2007; 188:139–144. [CrossRef]
42. Shin MS, Ho KJ. Clinical significance of azygos vein enlargement: radiographic recognition and etiologic analysis. Clin Imaging 1999; 23:236–240. [CrossRef]
43. Ko SF, Huang CC, Lin JW, et al. Imaging features and outcomes in 10 cases of idiopathic azygos vein aneurysm. Ann Thorac Surg 2014; 97:873–878. [CrossRef]
44. Koc Z, Oguzkurt L. Interruption or congenital stenosis of the inferior vena cava: prevalence, imaging, and clinical findings. Eur J Radiol 2007; 62:257–266. [CrossRef]
45. Lewis RB, Mehrotra AK, Rodriguez P, Levine MS. From the radiologic pathology archives: esophageal neoplasms: radiologic-pathologic correlation. Radiographics 2013; 33:1083–1108. [CrossRef]
46. Krasna MJ. Radiographic and endosonographic staging in esophageal cancer. Thorac Surg Clin 2013; 23:453–460. [CrossRef]
47. Botet JF, Lightdale C. Endoscopic sonography of the upper gastrointestinal tract. AJR Am J Roentgenol 1991; 156:63–68. [CrossRef]
48. van Rossum PS, van Hillegersberg R, Lever FM, et al. Imaging strategies in the management of oesophageal cancer: what's the role of MRI? Eur Radiol 2013; 23:1753–1765. [CrossRef]
49. Wong R, Walker-Dilks C, Raifu A. Evidence-based guideline recommendations on the use of positron emission tomography imaging in oesophageal cancer. Clin Oncol (R Coll Radiol) 2012; 24:86–104. [CrossRef]
50. Kwee RM. Prediction of tumor response to neoadjuvant therapy in patients with esophageal cancer with use of 18F FDG PET: a systematic review. Radiology 2010; 254:707–717. [CrossRef]
51. Bhatia V, Tajika M, Rastogi A. Upper gastrointestinal submucosal lesions--clinical and endosonographic evaluation and management. Trop Gastroenterol 2010; 31:5–29.
52. Tateishi U, Muller NL, Johkoh T, et al. Primary mediastinal lymphoma: characteristic features of the various histological subtypes on CT. J Comput Assist Tomogr 2004; 28:782–789. [CrossRef]
53. Takamizawa A, Koizumi T, Fujimoto K, et al. Primary malignant lymphoma in the posterior mediastinum. Respiration 2004; 71:417–420. [CrossRef]
54. Takahashi K, Al-Janabi NJ. Computed tomography and magnetic resonance imaging of mediastinal tumors. J Magn Reson Imaging 2010; 32:1325–1339. [CrossRef]
55. Cheson BD, Pfistner B, Juweid ME, et al. Revised response criteria for malignant lymphoma. J Clin Oncol 2007; 25:579–586. [CrossRef]
56. Glazer GM, Gross BH, Quint LE, Francis IR, Bookstein FL, Orringer MB. Normal mediastinal lymph nodes: number and size according to American Thoracic Society mapping. AJR Am J Roentgenol 1985; 144:261–265. [CrossRef]
57. Sharma A, Fidias P, Hayman LA, Loomis SL, Taber KH, Aquino SL. Patterns of lymphadenopathy in thoracic malignancies. Radiographics 2004; 24:419–434. [CrossRef]
58. Savoy AD, Ravenel JG, Hoffman BJ, Wallace MB. Endoscopic ultrasound for thoracic malignancy: a review. Curr Probl Diagn Radiol 2005; 34:106–115. [CrossRef]
59. Munden RF, Nesbitt JC, Kemp BL, Chasen MH, Whitman GJ. Primary liposarcoma of the mediastinum. AJR Am J Roentgenol 2000; 175:1340. [CrossRef]
60. O'Sullivan P, O'Dwyer H, Flint J, Munk PL, Muller N. Soft tissue tumours and mass-like lesions of the chest wall: a pictorial review of CT and MR findings. Br J Radiol 2007; 80:574–580. [CrossRef]
61. Molinari F, Bankier AA, Eisenberg RL. Fat-containing lesions in adult thoracic imaging. AJR Am J Roentgenol 2011; 197:W795–W813. [CrossRef]
62. Glazer HS, Wick MR, Anderson DJ, et al. CT of fatty thoracic masses. AJR Am J Roentgenol 1992; 159:1181–1187. [CrossRef]
63. Boiselle PM, Rosado-de-Christenson ML. Fat attenuation lesions of the mediastinum. J Comput Assist Tomogr 2001; 25:881–889. [CrossRef]
64. Kohn GP, Price RR, DeMeester SR, et al. Guidelines for the management of hiatal hernia. Surg Endosc 2013; 27:4409–4428. [CrossRef]
65. Andrici J, Tio M, Cox MR, Eslick GD. Hiatal hernia and the risk of Barrett's esophagus. J Gastroenterol Hepatol 2013; 28:415–431. [CrossRef]
66. Godwin JD, MacGregor JM. Extension of ascites into the chest with hiatal hernia: visualization on CT. AJR Am J Roentgenol 1987; 148:31–32. [CrossRef]
67. Temizoz O, Genchellac H, Yekeler E, et al. Prevalence and MDCT characteristics of asymptomatic Bochdalek hernia in adult population. Diagn Interv Radiol 2010; 16:52–55.
68. Garofano-Jerez JM, Lopez-Gonzalez Jde D, Valero-Gonzalez MA, Valenzuela-Barranco M. Posterolateral Bochdalek diaphragmatic hernia in adults. Rev Esp Enferm Dig 2011; 103:484–491. [CrossRef]
69. Sandstrom CK, Stern EJ. Diaphragmatic hernias: a spectrum of radiographic appearances. Curr Probl Diagn Radiol 2011; 40:95–115. [CrossRef]
70. Eren S, Ciris F. Diaphragmatic hernia: diagnostic approaches with review of the literature. Eur J Radiol 2005; 54:448–459. [CrossRef]
71. Brown SR, Horton JD, Trivette E, Hofmann LJ, Johnson JM. Bochdalek hernia in the adult: demographics, presentation, and surgical management. Hernia 2011; 15:23–30. [CrossRef]
72. Hajhosseini B, Montazeri V, Hajhosseini L, Nezami N, Beygui RE. Mediastinal goiter: a comprehensive study of 60 consecutive cases with special emphasis on identifying predictors of malignancy and sternotomy. Am J Surg 2012; 203:442–447. [CrossRef]
73. Algin O, Gokalp G, Topal U. Signs in chest imaging. Diagn Interv Radiol 2011; 17:18–29.
74. Mercante G, Gabrielli E, Pedroni C, et al. CT cross-sectional imaging classification system for substernal goiter based on risk factors for an extracervical surgical approach. Head Neck 2011; 33:792–799. [CrossRef]
75. Ross DS. Evaluation of the thyroid nodule. J Nucl Med 1991; 32:2181–2192.
76. Qureishi A, Garas G, Tolley N, Palazzo F, Athanasiou T, Zacharakis E. Can pre-operative computed tomography predict the need for a thoracic approach for removal of retrosternal goitre? Int J Surg 2013; 11:203–208. [CrossRef]

77. Bradley EL, 3rd. A clinically based classification system for acute pancreatitis: Summary of the International Symposium on Acute Pancreatitis, Atlanta, Ga, September 11 through 13, 1992. Arch Surg 1993; 128:586–590. [CrossRef]

78. Bhasin DK, Rana SS, Chandail VS, Nanda M, Sinha SK, Nagi B. Successful resolution of a mediastinal pseudocyst and pancreatic pleural effusion by endoscopic nasopancreatic drainage. JOP 2005; 6:359–364.

79. Sheu Y, Furlan A, Almusa O, Papachristou G, Bae KT. The revised Atlanta classification for acute pancreatitis: a CT imaging guide for radiologists. Emerg Radiol 2012; 19:237–243. [CrossRef]